Characterization of semiconductors from photoconductivity techniques: uniform and polychromatic illumination

Christophe Longeaud, Javier Schmidt, Jean-Paul Kleider

3

Characterization of semiconductors from photoconductivity techniques: uniform and polychromatic illumination

Christophe Longeaud[1,2], Javier Schmidt[3] and Jean-Paul Kleider[1]

[1] Group of Electrical Engineering – Paris (GeePs), CNRS, CentraleSupelec, Université Paris-Saclay, Sorbonne Université, 11 rue Joliot Curie, 91190 Gif sur Yvette, France

[2] Institut Photovoltaïque d'Île-de-France (IPVF), 18 Bd Thomas Gobert, 91120 Palaiseau, France

[3] Instituto de Física del Litoral (IFIS–Litoral), CONICET-UNL, Güemes 3450, S3000GNL Santa Fe, Argentina

Abstract

In this chapter we present optoelectronic characterization techniques that can be applied to coplanar samples as well as solar devices. Using the photoconductive properties of the semiconductor, the carrier generation is achieved with several photon energies lower than the band gap width of the material under investigation. These techniques are the constant photocurrent method (CPM) and the Fourier transform photocurrent spectroscopy (FTPS). The CPM was developed to gain information on the optical absorption of a semiconductor in an energy range where the sensitivity of the classical UV-visible spectroscopy is too low for this technique to be applicable. First, we present the theoretical and experimental bases of the CPM. Then, we show that the optical absorption is linked to the density of states (DOS) in the gap of the material and we present some of the models that were used to extract this DOS from the CPM results. Finally, we underline some of the limits of the CPM technique. One the main drawback of the CPM is the time needed for the acquisition of the variations of the absorption coefficient as function of the photon energy. The FTPS was imagined to overcome this drawback and, indeed, the same spectrum can be obtained within a few seconds. We present the theoretical and experimental bases of the FTPS and show that this technique can be used as a systematic mean of characterization of materials and devices replacing advantageously the CPM. To illustrate the powerfulness of the FPTS we give experimental results obtained on a solar device and compare them to the spectrum obtained on the device absorber. We conclude by presenting some results obtained by FTPS on perovskites, a very promising material for the future development of solar energy.

Keywords: photoconductivity, optical absorption, constant photocurrent method, Fourier transform photocurrent spectroscopy, density of states, perovskite, solar devices

3.1. Introduction

As shown in the previous chapter, valuable information can be obtained from the photoconductive properties of semiconductors with experiments performed on coplanar samples using a uniform and monochromatic illumination the photon energy of which is slightly larger than the band gap of the studied material. In this chapter, we shall show that complementary information can be obtained on the same materials from a uniform illumination with photon energies $h\nu$ lower than the band gap. The techniques developed on this basis aim at the determination of the absorption coefficient α of the material in an energy range where it is considered as 'transparent'. This means that the classical UV-visible spectroscopy cannot detect the very small changes of the absorption coefficient with the photon energies. However, the techniques developed have sensitivities orders of magnitude higher than the UV-visible spectroscopy and investigations on the variations of $\alpha(h\nu)$ on a large below-gap energy range were made possible. Optical absorption below the absorption edge can give fundamental information on the density of states (DOS) in the band gap. Indeed, for states located in the gap, the absorption is linked to the transitions of electrons from occupied states toward empty ones. Therefore, the precise determination of the absorption coefficient at low energies of photons should bring useful information on the defects of the studied semiconductor.

Several techniques have been developed for this purpose and applied to thin films. Among these, we can quote the Photothermal Deflection Spectroscopy (PDS), or "mirage effect", developed by A. Boccara *et al*. [1], as well as the Constant Photocurrent Method (CPM), first proposed by H. Grimmeiss and L. Lebedo [2] and applied to thin film semiconductors by M. Vaněček *et al*. in 1981 [3]. These two techniques do not lead systematically to the same results [4]. Indeed, CPM is mainly sensitive to the transitions generating carriers in the extended states, whereas PDS reveals all the transitions from occupied states toward empty ones, as, for instance, intra-gap transitions. Besides, PDS is very sensitive to the surface states.

In a first part we shall concentrate on the CPM that was successfully applied to many thin film materials such as hydrogenated amorphous silicon (a-Si:H), nano and micro crystalline silicon, …[3 - 9]. We shall present the basic principle of this technique which consists in maintaining the photocurrent constant while changing the photon energy. Then, after presenting the experimental set-up we shall show some experimental results and the different procedures that were suggested to extract information on the DOS of the studied material, as well as the limits of this technique.

However, though CPM can bring valuable information on the optoelectronic properties of thin film materials, it presents a main drawback to be used as a systematic characterization technique. The adjustment of the flux to maintain the photocurrent constant is time consuming and it may take a few hours to record a complete spectrum from say 0.8 eV to 2 eV (1550 – 620 nm). In addition, the wavelength resolution of the spectrum is limited by the monochromator resolution and, currently, the wavelength step is chosen of the order of 10 nm. To overcome these two issues, A. Poruba and M. Vaněček have proposed to use the light delivered by an FTIR spectrometer and to treat the sample response with Fast Fourier Transform (FFT) [10, 11]. This new technique, the Fourier Transform Photocurrent Spectroscopy (FTPS), based on the work of other groups [12, 13], proved to be very efficient on µc-Si thin films and devices, as well as on organic thin films [14]. A detailed overview of the technique has been proposed by J. Holovsky [15]. We present in a second part the bases of this Fourier transform analysis and, after presenting an experimental set-up, we show that it can be applied to solar devices and various materials, such as perovskites, to investigate their optoelectronic properties.

3.2. The constant photocurrent method (CPM)

3.2.1 CPM principle

To describe the basis of CPM we shall consider a photoconductive material in which a steady illumination generates holes and electrons. In this case an expression of the photoconductivity σ at a depth x from the illuminated surface of the film is given by

$$\sigma(x) = q\,(\mu_n\,\Delta n(x)+\mu_p\Delta p(x)) = q\,G(x)\;\eta(\mu_n\tau_n+\mu_p\tau_p) \quad , \qquad (3.1)$$

where q is the absolute value of the electron charge, μ_n (μ_p) is the electron (hole) extended state mobility, Δn (Δp) is the excess concentration of electrons (holes) compared to dark situation, $G(x)$ is the generation rate, η is the quantum efficiency and τ_n (τ_p) is the electron (hole) lifetime which we assume weakly dependent on x. Experimentally, a macroscopic photoconductivity σ is measured that can be considered as an average over the thickness d of the film of $\sigma(x)$, and, assuming a reflection coefficient R for the film, σ can be linked to an average value of $\eta(\mu_n\tau_n+\mu_p\tau_p)$ calculated from an average value of the generation rate in the sample

$$G = \frac{1}{d}\int_0^d G(x)\,dx = \frac{1}{d}(1-R)F(1-\exp(-\alpha d)) \quad , \qquad (3.2)$$

where F is the photon flux. An expression of the mean photoconductivity is then

$$\sigma = \frac{q}{d}\eta\left(\mu_n\tau_n + \mu_p\tau_p\right)(1-R)F(1-\exp(-\alpha d)) \quad . \qquad (3.3)$$

For low α values or small values of d, such as $\alpha d \ll 1$, Eq. (3.3) simplifies into

$$\sigma = q\;\eta(\mu_n\tau_n+\mu_p\tau_p)\,(1\text{-}R)\,F\,\alpha \quad . \qquad (3.4)$$

During CPM measurements the sample is illuminated at normal incidence by a monochromatic light (modulated or not) and the incident flux is varied when the photon energy $h\nu$ is changed so as to maintain the photocurrent constant on the whole range of explored wavelengths. The parameters η, R and μ_n are only weakly dependent on the photon energy [16] and it is assumed that, the photocurrent being constant, the splitting of the quasi Fermi levels stays constant during the experiment. Consequently, the recombination and the lifetimes remain constant and the dependence of α on photon energy obtained from the CPM technique, which will be denoted $\alpha_{CPM}(h\nu)$ can be deduced from

$$\alpha_{CPM}(h\nu) = \frac{K}{F(h\nu)} \quad , \qquad (3.5)$$

where K is a constant. This constant is unknown, therefore the CPM technique can only provide relative variations of the absorption coefficient, while absolute values require a calibration procedure using for instance transmission/reflection measurements as it will be detailed later.

We present in Fig 3.1 the possible transitions from filled states toward empty ones induced by absorption of a photon with an energy lower than the band gap in a-Si:H. In this schematic picture the a-Si:H DOS is represented by two exponential band tails and two Gaussian distributions for the deep states. Only the transitions A and B, generating free holes and electrons, will be seen by the CPM since this technique is based on the measurement of a photocurrent. Transition C will not generate any current but could be seen by PDS. It explains why, in most of the cases, both techniques do not give the same results, PDS being sensitive to transitions unseen by CPM.

Fig. 3.2 displays a schematic diagram of a CPM bench. The light comes from a halogen lamp and is focused with lenses on the entrance of a monochromator. Other lenses are adapted at the exit of the monochromator to give a beam of parallel light. Optical filters are also fixed at the exit of the monochromator to eliminate the higher wavelength orders of the light, if necessary, to eventually end with the desired wavelength. The sample is set inside a cryostat fixed to X-Y movable plates to optimize the film illumination. A beam splitter, the transmission and reflection of which have been calibrated, transmits a part of the light to the sample and reflects another part toward calibrated photodiodes. Knowing the optical characteristics of the beam splitter and the spectral responses of the photodiodes, it is possible to deduce the flux impinging the film. The photodiodes are either a c-Si diode for the visible and very near infrared range (400 – 1100 nm) or a c-Ge diode for the 800 – 1750 nm range of wavelengths. The currents generated by the photodiodes are measured with an electrometer.

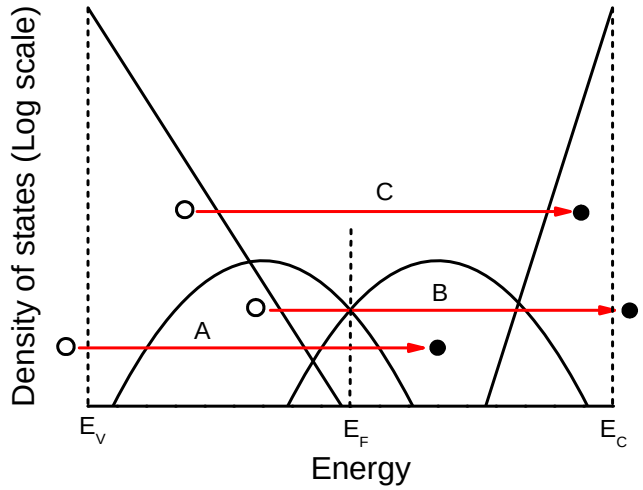

Figure 3.1. Schematic picture of the density of states in the band gap of a-Si:H, emphasizing possible electronic transitions induced by a photon of energy lower than the band gap. Transition A generates holes in the valence band, transition B generates electrons in the conduction band and transition C is an intra-band transition. E_V (E_C) is the energy of the top (bottom) of the valence (conduction) band, and E_F is the Fermi level.

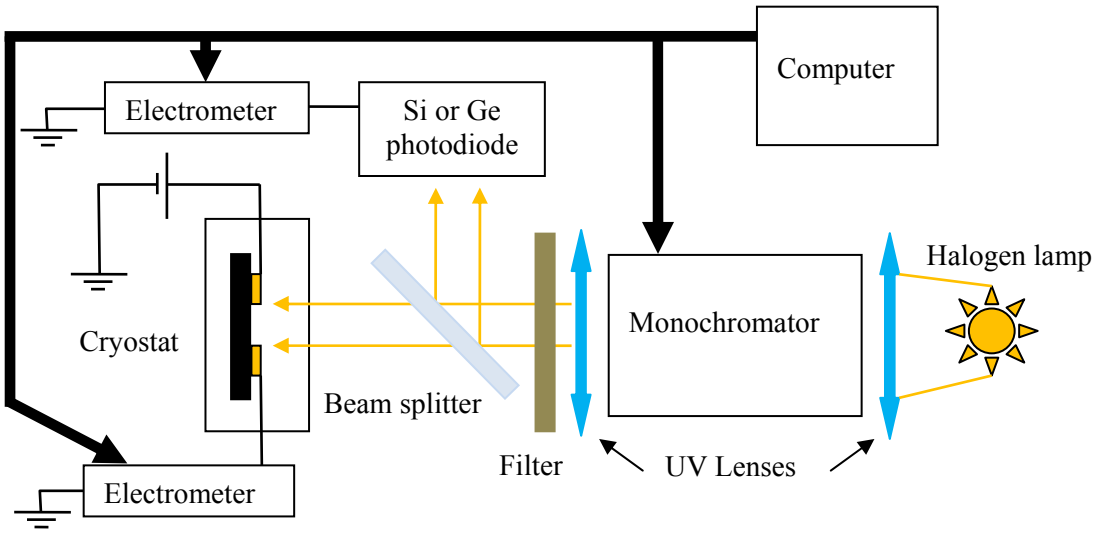

Figure 3.2. Schematic diagram of a CPM bench

To obtain a CPM spectrum one first measures by means of an electrometer the dark current I_{dark} flowing between the two coplanar electrodes due to the applied DC voltage. Then, one illuminates the sample with the highest wavelength available, say λ_0, and with the highest flux, say F_0, and from the total current I_T the photocurrent is deduced: $I_{ph} = I_T - I_{dark}$. Then, the wavelength is decreased to λ_1 and the flux adjusted to a value F_1 until the same I_{ph} is obtained. The adjustment of the flux is achieved

by playing with the slits at the exit of the monochromator and with the current controlling the intensity of the halogen lamp. This procedure is repeated for i different wavelengths until the lowest final wavelength is reached. The variations of $\alpha_{CPM}(\lambda_i)$ are deduced from the plot of $1/F(\lambda_i)$ according to Eq. (3.5).

As mentioned above, the CPM gives only access to the relative variations of the below-gap absorption coefficient. To deduce the absolute variations of α one has to perform transmission/reflection measurements, from which it is possible to have the absolute values of α in a limited range of photon energies close to the band edge. Subsequently, the absolute variations of α_{CPM} are deduced by adjusting the CPM spectrum to the spectrum deduced from UV-visible spectroscopy, meaning that the constant K in Eq. (3.5) is adjusted so that the α values deduced from CPM match the spectrum obtained from UV-visible spectroscopy in the energy range where this latter provides reliable data. As a matter of example, we present in Fig. 3.3 the calibration of a CPM spectrum of a polymorphous hydrogenated silicon (pm-Si:H) sample to its transmission/reflection spectrum. The interest of the CPM is obvious on this curve, where it can be seen that the CPM explores the α variations over 5 orders of magnitude when the transmission/reflection spectrum can be accurately probed over only 2 orders of magnitude. This exploration of the absorption coefficient reveals the well-known DOS of the pm-Si:H made of deep defects below 1.4 eV (part 1) and an exponential band tail above (part 2) with a characteristic energy, or Urbach energy, of the order of E_u = 58 meV in the present case. Since pm-Si:H is slightly n-type the photoconductivity is dominated by electrons. So it is expected, and numerical simulations have confirmed, that this band tail is linked to the valence band tail (VBT) of the material, which is larger than the conduction band tail. That is why the CPM experiment is complementary to the ones presented in the previous chapter that were mainly sensitive to the states located in the upper part of the gap, above the Fermi level.

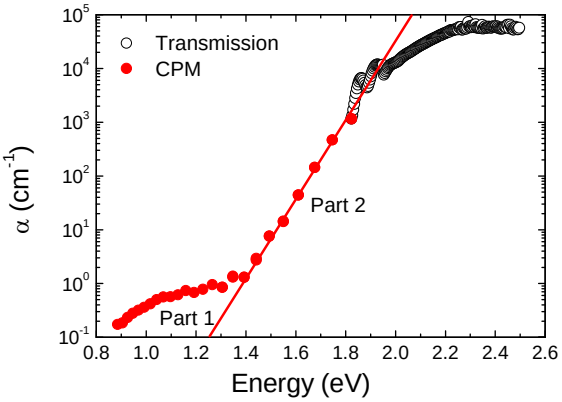

Figure 3.3. CPM absorption spectrum (red circles) calibrated to the corresponding transmission/reflection spectrum (black open circles) to give the below-gap variations of α in a pm-Si:H sample. The straight line shows that α is varying exponentially in Part 2, reflecting the exponential tail states in this material.

3.2.2 Absolute CPM

To avoid the problem of calibrating the CPM curves to obtain absolute values of α, M. Vaněček *et al.* have proposed a method called "absolute CPM" (ACPM) [17]. This method is applicable to materials for which the optical parameters, as maximum transmission, reflection coefficients from the film side, or from the glass side when the film is deposited on glass, are rather constant from one film to another and well known from optical measurements. In this method, in addition to the measurement of the impinging flux as described above, one measures the flux transmitted through the film. M. Sasaki *et al.* and Y. Hishikawa *et al.* had proposed to use the transmitted flux instead of the direct flux to derive the variations of the absorption coefficient, for this method (Transmission CPM, TCPM) has the advantage of being more precise, suppressing the

interferences that are sometimes seen on the CPM spectrum and that blur the results [18, 19]. Vaněček *et al.* proposed to use the ratio of the transmitted flux over the direct flux (T/D) to derive the transmission curve. In the case of a-Si:H deposited on the glass usually used for photovoltaic devices, the transmission in the weak absorption region is well known and reaches maximum values of the order of $T = 0.92$. Knowing this value allows to correct for small inaccuracies in the T/D measurement. In the strong absorption region the interferences and the transmission tend toward 0, and for a photon energy $h\nu_0$ where the interferences are absent one can deduce the absorptance A from the relation $A = 1\text{-}T(h\nu_0)\text{-}R$, with $R = 0.41$ if the sample is illuminated from the film side or $R = 0.26$ if the sample is illuminated from the glass side [17]. It is then possible to calculate the ratio A/T for this particular energy $h\nu_0$ and, subsequently, to deduce the absolute values of the variations of $A/T(h\nu)$ on the complete range of explored energies from the α_{CPM} spectrum calculated with Eq. (3.5) in which the flux used is the transmitted one. Indeed, this spectrum is proportional to A/T. Following D. Ritter and K. Weiser, assuming that the reflection coefficient is almost constant in the range of explored energies, it is finally possible to deduce the absolute variations of the absorption coefficient from [20]

$$\alpha(h\nu)d = \ln\left(\frac{(1-R)\left(1+\frac{A}{T}(h\nu)\right)+\sqrt{(1-R)^2\left(1+\frac{A}{T}(h\nu)\right)^2+4R}}{2}\right) \quad . \qquad (3.6)$$

This procedure was successfully used to obtain the absolute variations of the below-gap absorption coefficient of a-Si:H thin films as well as nano and microcrystalline silicon without the necessity to calibrate the CPM curve with optical measurements. It could be easily applied to other thin film materials provided their optical parameters, such as R and T, are well known. We present in Fig. 3.4 three different spectra of the below-gap absorption coefficient measured on a light-soaked pm-Si:H sample and calculated from Eq. (3.5) using either the direct flux (black circles), or the transmitted flux (red triangles), both calibrated according to the spectrum deduced from the ACPM technique (blue stars). It can be seen that: i/ with the direct flux the spectrum is inaccurate because of interferences, ii/ the use of the transmitted flux results in an increase of the α_{CPM} values deduced from Eq. (3.5) and, hence, on the α values at high energies for the transmission becomes very small, and iii/ the ACPM technique gives a spectrum almost free of interferences.

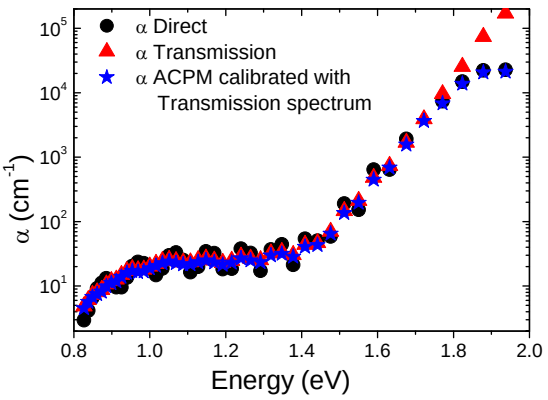

Figure 3.4. CPM absorption spectra measured on a light-soaked pm-Si:H sample with normalization to the direct flux (black circles), normalization to the transmitted flux (red triangles) compared with the absorption spectra obtained from ACPM (blue stars). The α Direct and α Transmission spectra have been normalized to the ACPM spectrum for comparison.

3.2.3 Determination of the DOS from a CPM spectrum

The CPM spectrum gives information on the below-gap absorption coefficient and, consequently, should give information on the DOS responsible for it. In this respect several models have been developed to extract the DOS distribution from the CPM data. These models have been

essentially developed for a-Si:H, pm-Si:H and hydrogenated microcrystalline silicon (µc-Si:H) thin films, but can be applied to any type of thin film material. Different approaches have been proposed to estimate the deep gap states distribution and concentration from a CPM spectrum: deconvolution of the CPM spectrum, calculation of the excess absorption and use of a single α value at a chosen energy.

3.2.3.a *Deconvolution of a CPM spectrum*

This deconvolution is based on the theoretical expression of α, which is written as the convolution product between the initial occupied states, $N_i(E\text{-}h\nu)$, and the final empty states, $N_f(E)$, between which optical transitions of carriers occur when photons of energy $h\nu$ are absorbed,

$$\alpha(h\nu) = \frac{C}{h\nu}\int N_i(E - h\nu) f_i\,(E - h\nu) N_f(E)[1 - f_f(E)]dE \quad , \qquad (3.7)$$

where C is a constant including the square of the optical matrix element, assumed to be constant for all the transitions, $f_i(E\text{-}h\nu)$ and $f_f(E)$ are the occupation functions of the initial and final states, respectively, and the integral is taken over the whole possible transitions, i.e., $E_V\text{-}h\nu$ and $E_C\text{+}h\nu$, where E_V (E_C) is the energy of the top (bottom) of the valence (conduction) band. In the work of M. Vaněček the coefficient C was taken equal to 4.34×10^{-38} cm^{5}eV^2 [21]. Two procedures have been proposed.

The first procedure proposes a DOS model, uses Eq. (3.7) to calculate the absorption coefficient on an energy range identical to the experimental one, and compares the final result to the experimental data [22]. One can play with the DOS parameters until a good match between experimental and calculated absorption is found. The choice of a DOS can be controversial but most of the models are based on one or two Gaussian distribution(s) for the deep states and exponentially varying valence and conduction band tails. The most controversial point is the choice of the optical and thermal transition coefficients needed to calculate the occupation functions, and several values for the coefficient C can be found in the literature leading to different results [22, 23].

The second method does not make any assumption on the defect distribution [24, 25] but assumes that the DOS is constant above E_C. K. Pierz *et al.* calculate first $D = \mathrm{d}\alpha/\mathrm{d}(h\nu)$ and then the DOS distribution from $N(E_C - h\nu) = M\times D$, where $M = 1.6\times10^{24}(h\nu\times R^2 N_C)$, R^2 being the square of the matrix element and N_C the equivalent density of states at the bottom of the conduction band. Though this procedure is very simple, it is based on a hardly sustainable assumption: a constant value for the DOS above E_C. In addition, even if one takes into account the variation of the DOS with energy above E_C, as P. Jensen did [26], the determination of the DOS is still linked to the value of the M coefficient that remains unknown.

3.2.3.b *Calculation of the excess absorption*

W. B. Jackson and N. Amer have proposed a simple method to determine the deep defect concentration from PDS spectra [27]. This technique can be extended to the CPM spectra, and consists in integrating the "excess" absorption defined as the difference between the total absorption, α_{Tot}, and the absorption due to the band tail states, α_{Urbach}. In the case of a-Si:H, this absorption was calibrated from Electron Spin Resonance (ESR) data by Z. Smith *et al.* [4] leading to

$$N_D = 1.9\times10^{16}\int_{E_1}^{E_2}(\alpha_{Tot} - \alpha_{Urbach})dE \quad , \qquad (3.8)$$

where E_1 is the lowest photon energy and E_2 the energy of the onset of the band tail. In this formula, energies are expressed in eV, absorption coefficients in cm^{-1} and the resulting defect density is obtained in cm^{-3}.

This method was justified in the case of a-Si:H by the good correlation between the N_D values and the spin densities measured by ESR. However, the main criticism against this technique is that the defects probed by ESR are only the neutral ones and it ignores the charged defects, such as those predicted by the defect pool model [28, 29]. In addition, the determination of N_D strongly depends on the determination of E_u, the experimental value of which is often inaccurate.

3.2.3.c *Absorption at a single energy*

Another method used to estimate the deep defect concentration from the CPM data is to link the value of the absorption coefficient at a given energy to the defect concentration measured by another technique. In the case of a-Si:H, N. Wyrsch *et al.* have suggested to choose 1.2 eV as the reference energy [30], while some other groups suggested to choose the energy at which the band tail departs from the deep states [31]. N. Wyrsch *et al.* have found that, if the absorption coefficient at 1.2 eV was equal to 1 cm^{-1}, the deep defect density should be in the range $2.4\text{-}5\times10^{16}$ cm^{-3}. This calibration was done using the results of several groups using different techniques, including ESR. Once again, it can be seen that linking the deep defect density to the absorption coefficient is rather tricky and one cannot expect to extract defect densities with a better precision than a factor of 2.

3.2.4 Limits of the CPM

As mentioned above, the main CPM assumption is that maintaining the photocurrent constant results in a constant lifetime. However, with below-gap illumination the gap states occupancy may vary significantly depending on the excitation wavelength, generating an evolution of the recombination path and of the carrier lifetimes. This was demonstrated by J. Schmidt and F. Rubinelli [6] who have defined a complete model of the DOS, including amphoteric states as in the defect pool model, to calculate the true absorption coefficient α_{Tot} for intrinsic and doped a-Si:H. Then, they have compared α_{Tot} to the absorption coefficient that would be obtained from CPM, α_{CPM}. They have shown that, in a-Si:H and in the photon energy range 0.8 eV $\leq h\nu \leq$ 1.3 eV, α_{Tot} can be underestimated by α_{CPM} for some values of the capture coefficients. They have shown that, in this energy range, a modification of the electron lifetime can occur for some sets of capture coefficients even if one maintains the photocurrent constant. Hence, in this particular case the proportionality between $\alpha(h\nu)$ and $1/F(h\nu)$ is not fulfilled.

On the other hand, as far as the valence band tail is concerned and for photon energies larger than 1.3 eV, these authors have shown that one has $\alpha_{Tot} = \alpha_{CPM}$. Indeed, for $h\nu >$ 1.3 eV the carriers generated in the conduction band are mainly due to transitions from the VBT, the density of which is so high, compared to deep states, that a modification of the occupancy of these latter would not change the recombination path and thus the electron lifetime.

In addition, J. Schmidt and F. Rubinelli have investigated on two of the above-mentioned methods used to estimate the deep defect density: the integral of excess absorption and the absorption at a single energy. They have shown that these two methods underestimate the deep defect density, and that a change in defect distribution keeping a constant concentration of defects could lead to a large modification of the absorption coefficient.

Other authors have explored the CPM flaws under some experimental conditions [32, 33]. For instance, G. Conte *et al.* have shown that the CPM spectrum measured on a-Si:H depends on the level of current chosen to perform the experiment.

Finally, the CPM spectrum may depend on the structure of the sample. F. Siebke *et al.* have shown that, for microcrystalline samples, at high crystalline fraction the estimate of the absorption coefficient was rather reliable, whereas at low crystalline fraction the CPM underestimated the

absorption coefficient for energies lower than 1.7 eV [34]. According to these authors, this difference comes from the different paths opened to the current from one grain to another, these paths depending on the grain density (percolation path). Crystallites could also diffuse the impinging light, leading to a difficult estimate of the flux, particularly when this latter is measured after transmission through the sample. This influence of crystallites was also underlined by Poruba *et al.* [35].

3.2.5 AC CPM versus DC CPM

All the developments mentioned above concern the CPM performed with a DC illumination. Another drawback of this method, not mentioned yet, is the very low value of the photocurrent one has to deal with when the sample is illuminated with low energy photons. The difference between the total current and the dark current may be very small and noisy, adding uncertainties to the determination of the CPM spectrum. Working with an alternating flux is a way to get rid of this issue, for the AC current can be measured more accurately with a lock-in amplifier. However, discrepancies between the DC-CPM and AC-CPM were underlined by different groups [33, 36, 37]. In the low energy region, $h\nu < 1.4$ eV, differences in the CPM spectra between DC and AC measurements could even reach one order of magnitude, the DC spectrum being always higher than the AC one.

An explanation of these discrepancies was provided by C. Main *et al.*, who have compared experimental results with a numerical calculation based on a "standard DOS" of a-Si:H [38]. They have clearly demonstrated that the DC response includes transitions of carriers into unoccupied states above the Fermi level E_F, these carriers being subsequently thermally released toward the conduction band to produce free carriers. These last transitions act as a low pass filter when the experiment is performed in AC mode and, above a frequency limit of the order of 50 Hz according to these authors, the AC response is coming only from transitions from occupied states below the Fermi level. Their conclusion is that DC CPM describes correctly the absorption variations with photon energy, but the DOS is more accurately determined from the AC measurements. They have even proposed a method to determine the DOS of unoccupied states by subtracting the AC spectrum to the DC one. The combination of these two techniques would reveal the distribution of defects both below and above E_F. However, the contribution of holes was not taken into account in their model, and taking them into account may modify their conclusions.

In conclusion to this part, the CPM technique appears simple in its basic principle and was applied successfully to the optimization of thin film semiconductors. However, the precise determination of the DOS depends largely on the chosen model and, to some extent, on the way the experiment is performed. In addition, as mentioned in the introduction, the data acquisition is rather long (a few hours), which makes the CPM difficult to use as a systematic means of characterization. This drawback is completely suppressed with the Fourier transform photocurrent spectroscopy presented in the next section.

3.3. The Fourier-transform photocurrent spectroscopy (FTPS)

3.3.1 FTPS bases

The FTPS technique using an FTIR spectrometer is much less intuitive than dispersive spectroscopy. In an FTIR spectrometer, instead of a monochromatic beam, a broadband light beam containing many wavelengths is emitted from the output of a Michelson interferometer. A schematic diagram of a Michelson interferometer is presented in Fig. 3.5. The light source is a collimated halogen lamp illuminating a beam splitter. Part of the light is reflected toward a fixed mirror **F** and part is transmitted toward a movable mirror **M** perpendicular to the fixed one. The light reflected on

each mirror is sent back toward the beam splitter and finally merges into a single beam reaching a detector positioned on an axis perpendicular to the axis of the incoming light. Assuming that the beam splitter is perfect (50 % transmission and 50 % reflection) the intensity of the light reaching the detector depends on the wavelength and on the differences of optical paths between point O and the two mirrors **F** or **M**: $\delta = 2$ (OF-OM).

If we consider a monochromatic light of wavelength λ_0, when OF = OM the path difference is null (zero path difference) the two beams interfere constructively. A displacement of the movable mirror of $\lambda_0/4$ results in a difference of optical path of $\delta = \lambda_0/2$ and the two beams interfere destructively with no light transmitted toward the detector.

If we call ϕ the phase difference between the two interfering beams, an expression of the intensity of light reaching the detector can be written

$$I'(\delta) = \frac{I(\lambda_0)}{2}\{1 + \cos[\phi(\delta)]\} \quad , \qquad (3.9)$$

with

$$\phi = 2\pi\frac{\delta}{\lambda_0} \quad , \qquad (3.10)$$

where $I(\lambda_0)$ is the intensity of the light coming from the source. The main information on the light transmitted, or not, toward the detector is contained in the alternating part of Eq. (3.9) and we shall consider only this part in the following.

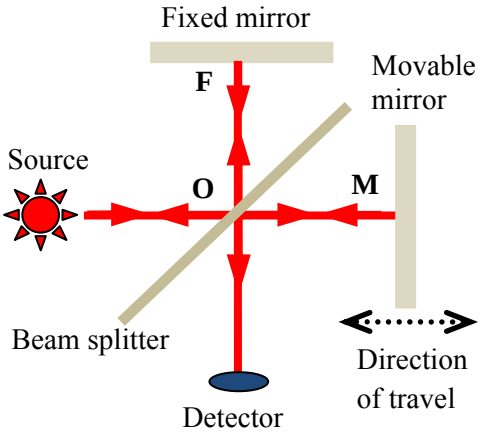

Figure 3.5. Schematic diagram of a Michelson interferometer.

Experimentally, the Michelson interferometer may not be an ideal one. For instance, the 50-50 transmission-reflection coefficients for the beam splitter may not be verified for all the wavelengths, and the reflection of the mirrors may not be strictly identical. It means that we have to take into account a "transfer function" $H(\lambda_0)$ for the Michelson interferometer. In addition, the response of the detector $R(\lambda_0)$ is often amplified and one has to take into account the "transfer function" $G(\lambda_0)$ of the amplifier. Introducing the wavenumber corresponding to λ_0, $\omega_0 = 1/\lambda_0$, and a global transfer function of the whole system $B(\omega_0) = H(\omega_0)G(\omega_0)/4$, the final global response $S(\delta)$ can be written

$$S(\delta) = \frac{H(\omega_0)G(\omega_0)R(\omega_0)}{2}\cos(2\pi\omega_0\delta) = 2B(\omega_0)R(\omega_0)\cos(2\pi\omega_0\delta) \quad . \qquad (3.11)$$

From the above expression it can be seen that $S(\delta)$ is the cosine part of a Fourier transform of $B(\omega_0)R(\omega_0)$.

When the light source is polychromatic, one has to sum all the contributions for all the wavelengths to obtain the global response that can be written as

$$S(\delta) = 2\int_0^{+\infty} B(\omega)R(\omega)\cos(2\pi\omega\delta)\,d\omega \quad , \qquad (3.12)$$

or, thanks to the parity of the cosine function,

$$S(\delta) = \int_{-\infty}^{+\infty} B(\omega)R(\omega)\cos(2\pi\omega\delta)\,d\omega \quad . \qquad (3.13)$$

The spectrum $B(\omega)R(\omega)$ can be obtained by an inverse Fourier transform to end with

$$B(\omega)R(\omega) = 2\int_0^{+\infty} S(\delta)\cos(2\pi\omega\delta)\,d\delta \quad . \qquad (3.14)$$

Theoretically, from Eq. (3.14) one should record the spectrum $B(\omega)R(\omega)$ from 0 to infinity with an infinitely high resolution. In practice, the range of displacement of the moving mirror is limited and the acquisition is done by sampling the detector response. These two limits have to be taken into account when performing the inverse Fourier transform.

Another point that has to be underlined is that the light reaching the detector is not steady. Indeed, the moving mirror is translated at a constant speed V. If we take the origin of time t when the difference of the optical paths is null, at any time we may write $\delta = 2Vt$, and Eq. (3.11) transforms into

$$S(\delta) = 2B(\omega_0)R(\omega_0)\cos(2\pi\omega_0 2Vt) \quad , \qquad (3.15)$$

from which we can define a characteristic frequency, known as the Fourier frequency, for the wavenumber ω_0

$$f(\omega_0) = 2V\omega_0 \quad . \qquad (3.16)$$

For instance, with a speed of $V = 0.16$ cm/s the Fourier frequency at 400 nm (1600 nm) equals 8 kHz (2 kHz).

In practice, the detector is replaced by the sample to be studied and the photocurrent coming out of it is treated by the FTIR, which takes into account the limits mentioned above and corrects the treatment of the data accordingly while performing a Fast Fourier Transform (FFT). This FFT being applied to voltage data, a current-voltage amplifier is placed after the sample to amplify the signal and convert it into a voltage treated subsequently by the FTIR. The bandwidth of the I-V amplifier must be chosen much larger than the maximum Fourier frequency to avoid a modification by the amplifier of the signal coming out of the sample. In addition, the noise inherent to the amplifier must be removed by recording a baseline (BL) when no light is sent to the sample. However, even after this subtraction, the final spectrum still contains the term $B(\omega)$, which is unknown

$$B(\omega)[R(\omega) - R_{\mathrm{BL}}(\omega)] = B(\omega)R_{\mathrm{sample}}(\omega) \quad . \qquad (3.17)$$

To get rid of the term $B(\omega)$ the sample can be replaced by a reference photodiode, the response of which is known. By performing the same measurement on this photodiode one can normalize the sample response to that of the photodiode, $R_{\mathrm{ref}}(\omega)$, this normalization being independent of the global transfer function $B(\omega)$

$$\frac{B(\omega)R_{\mathrm{sample}}(\omega)}{B(\omega)R_{\mathrm{ref}}(\omega)} = \frac{R_{\mathrm{sample}}(\omega)}{R_{\mathrm{ref}}(\omega)} \quad . \qquad (3.18)$$

The last point to address is the resolution of the FTIR measurements. The sampling step is usually 4 cm^{-1}. For large wavelengths, in the near infrared region, say around 1.8 µm, two consecutive wave numbers will be 5550 and 5554 cm^{-1}, for instance, and the wavelength resolution will be of the order of 1.3 nm. At the other end of the spectrum, say around 400 nm, two consecutive wave numbers will be 25000 and 25004 cm^{-1}, for instance, and the wavelength resolution will be of the order of 0.06 nm. Hence, even with a standard data spacing the resolution is largely better than with a dispersive measurement using a monochromator with a wavelength step of 10 nm.

In addition to this high resolution, one has to emphasize the rapidity of the data acquisition. Indeed, with a mirror moving at a speed of 0.16 cm/s it takes 1 s to record a full spectrum which makes the FTPS a very efficient technique, extremely rapid even if one averages the data 60 times to improve the signal to noise ratio, and that can be used as a systematic characterization technique for the optimization of photoconductive materials and devices.

3.3.2 FTPS bench

Different schematic diagrams of FTPS benches can be found in Refs. [11, 15, 39]. These benches have the main drawback to be very rigid since the optical components (*e.g.* parabolic mirror) used to shine light onto the sample and the sample itself are fixed. That is why we have built a setup, the diagram of which is displayed in Fig. 3.6.

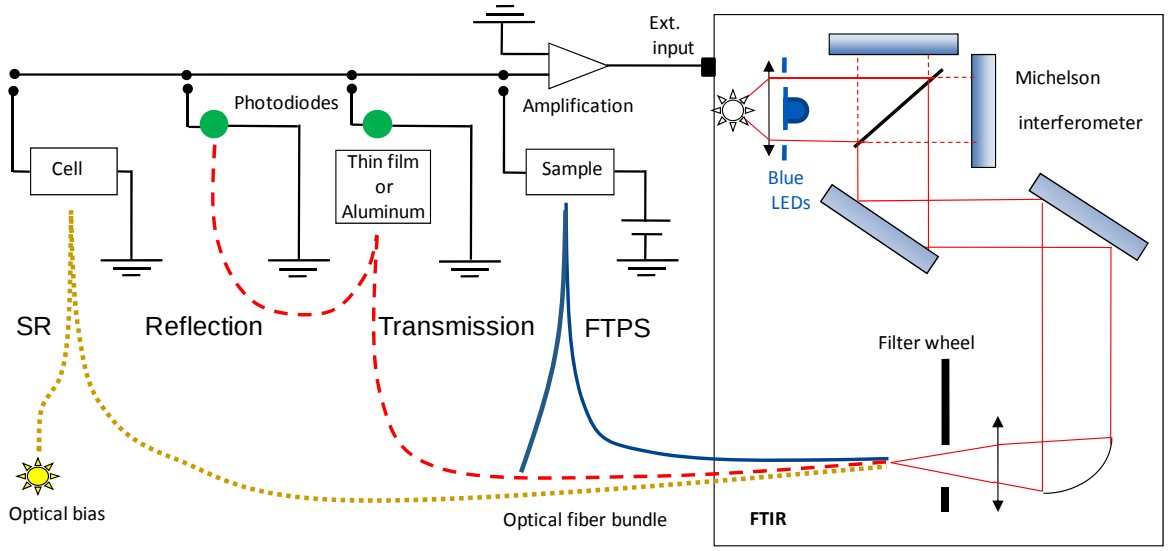

Figure 3.6. Schematic diagram of a versatile FTPS set-up. The blue full line, red dashed line and yellow dotted line represent the positions of the optical fiber bundle when performing the FTPS, reflection/transmission and spectral response (SR) experiments, respectively.

This setup allows implementing three characterization techniques with only very simple modifications of the system. Details of this bench can be found in [40]. To work in the visible and near infrared part of the spectrum all the FTIR mirrors are covered with aluminum and the beam splitter of the Michelson interferometer is a quartz plate. The light source is a halogen lamp to which we can add a LED source composed of five LEDs at 405, 420, 450, 470 and 532 nm. With this system we can cover easily a wavelength range from 390 to 1800 nm. In the sample compartment of the FTIR we have installed one branch of a bifurcated silica optical fiber bundle (input diameter 3.2 mm, numerical aperture NA = 0.22) and concentrated the light exiting the Michelson interferometer with a silica lens (5 cm in diameter and a focal length of ≈ 5 cm) onto the input of this branch. The latter is set on a

XYZ mount to optimize the light collection. A filter wheel is inserted between the lens and the input of the optical fiber to select ranges of light energies if needed. The advantage of this system is that the output of the optical fiber (4.7 mm in diameter, NA =0.22) can be moved in front of any type or size of sample or device fixed on a substrate holder, in the air or in a cryostat. The response of the sample is amplified by a low noise and large bandwidth current-voltage amplifier (50 kHz at a gain of 10^7 V/A) before being sent to an external input of the FTIR to be treated by FFT. To measure the intensity of the light impinging or going through the studied samples, we use two calibrated photodiodes: a 1 cm^2 crystalline silicon (c-Si) photodiode in the 390 – 1100 nm range and a 1 cm^2 crystalline germanium (c-Ge) photodiode in the 800 - 1800 nm range.

As mentioned, three different characterizations can be done with this system. For the FTPS the sample is usually a coplanar film deposited onto a transparent substrate (*e.g.* glass) and fitted with two parallel electrodes 1 mm apart and 1 cm long. The sample is fixed onto an electronic circuit plate by two springs that both maintain it mechanically and connect the electrodes to the amplifier and a bias source. A small slit, 0.8 mm wide and 5 mm high, was drilled in the substrate holder. This way it is possible to measure the flux of the light shone onto the sample using the substrate holder alone and placing a calibrated photodiode immediately behind it. It is also possible to measure the flux of light transmitted through the film once fixed onto the substrate holder, the slit being aligned with the electrode spacing. Thus, the FTPS spectra can be deduced from the response of the sample normalized, according to Eq. (3.18), with the flux of light impinging the sample or with the flux of light transmitted through the film, and the same procedure as for the 'absolute CPM' [17] can be followed to achieve an 'absolute FTPS' measurement.

Reflectance measurements can also be achieved on thin films without any electrodes. The fiber bundle being bifurcated, it is possible to record the reflectance of the sample by collecting the light reflected by the sample and transmitted by the second branch of the bundle toward a photodiode. The calibration is performed by replacing the sample by an aluminum mirror, the reflectance of which has been measured previously. From these reflection/transmission measurements it is possible to deduce optical parameters of the film, such as the refractive index, the thickness and the absorption coefficient $\alpha(h\nu)$ in the high photon energy region, using the theoretical developments proposed by Poruba *et al.* [35]. The measurement of $\alpha(h\nu)$ can also be used to set the FTPS spectra to their absolute values, as it is done with CPM.

Finally, spectral responses of devices can be performed, replacing the coplanar film by the corresponding device. In some cases, as for tandem cells, for instance, it is possible to use the second branch of the fiber bundle to add a bias of light to the FTIR light. We will not detail this option of the bench we have designed because it is beyond the scope of this chapter.

3.3.3 Experimental results

3.3.3.a *Comparison of calibrations with transmitted or direct flux*

In Fig. 3.7a we present the FTPS spectra obtained on an a-Si:H thin film. The corresponding absorption coefficient is shown in Fig. 3.7b. Different colors were used to illustrate the different acquisitions performed to record the FTPS spectra. The spectra were obtained by normalization of the sample response with Eq. (3.18), either with the direct flux (black and green full lines) or with the transmitted flux (red and blue full lines). Two colors are used to display each spectrum normalized to direct or transmitted flux because the experiment is achieved in two steps. In a first step, the current flowing through the sample is measured with the full spectrum of light and the flux is calibrated with the c-Si photodiode. Since the dynamic range of the measurement is a little bit more than 5 decades (see Fig. 3.7), it is impossible to use the same gain of the amplifier to record the complete spectrum, the contribution to the current of the transitions from the deepest states being too low. To amplify this

contribution, the light of the FTIR is filtered below 746 nm to suppress the high energy photons. The gain of the amplifier can then be increased to obtain the contribution to the current of the deepest states with a good signal to noise ratio. In addition, in this low energy range the normalization of the FTPS is performed by measuring the flux with the c-Ge photodiode.

We can do the same remarks on the FTPS spectra as previously done on the CPM spectra presented in Fig. 3.4. The spectra obtained by normalization with the direct flux exhibit a strong influence of the interferences, which is largely decreased when the normalization is done with the transmitted flux. In the high energy region, the FTPS spectrum normalized with transmission is increasing steeply because the transmitted flux tends toward 0 in this energy region. Combining these two measurements with that of the transmittance, it was possible to derive an 'absolute FTPS' spectrum that should describe the absorption coefficient variations in an absolute scale, as shown in Fig. 3.7b. From the usual and simple definition of an "optical" band gap, E_{04}, defined as the energy for which $\alpha = 10^4$ cm^{-1}, it can be seen that the a-Si:H film studied here presents a large E_{04} gap equal to 1.95 eV, and a rather large Urbach energy $E_u = 69$ meV.

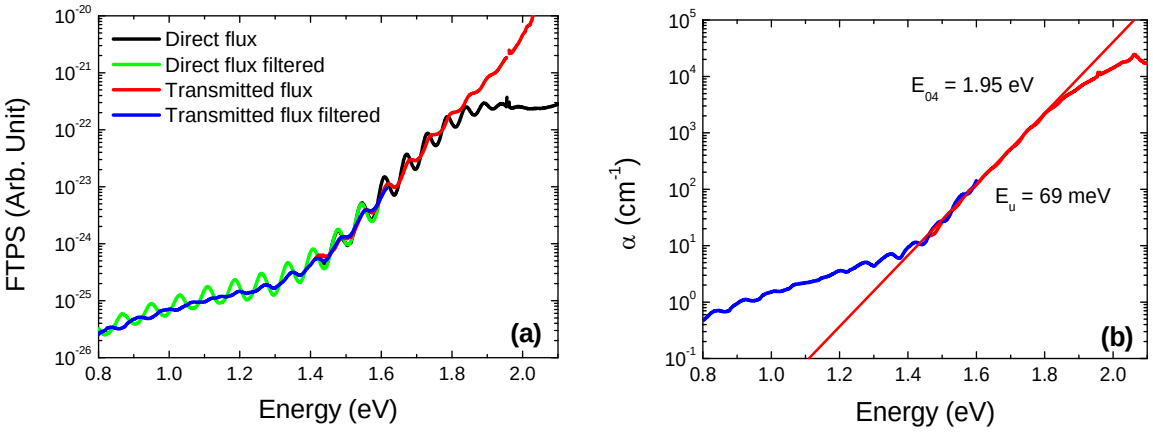

Figure 3.7. (a) FTPS spectra measured on an a-Si:H film with normalization to the direct flux, with or without a filter at 746 nm, green and black lines, respectively, or normalization to the transmitted flux, with or without a filter at 746 nm, blue and red lines, respectively, and (b) the deduced absorption coefficient.

Though these results appear very similar to what we would have obtained with CPM, there might be some slight differences. Indeed, as mentioned in the previous section on CPM, we may expect differences in the estimate of the variations of the absorption coefficient measured in AC CPM and DC CPM. In FTPS we have a constant background of light, since almost all the wavelengths are present at the same time in the excitation light, and we may expect to have constant mobility × lifetime products. However, this background is not a steady one, as it would be the case with Dual Beam Photoconductivity (DBP) [41], because it is made of a sum of alternating contributions, oscillating at a few kHz, for each wavelength. A comparison of the results obtained with different methods, AC CPM at low frequency (13 Hz) and FTPS, applied to the same samples and devices, was performed by J. Holovsky *et al.* It was found that these methods lead to different results, both on films and devices, especially for the deep states evaluation [42]. For the films, in the low energy region, it was found that the FTPS spectra were always slightly lower than the CPM ones, whereas the reverse prevailed for devices, with FTPS spectra slightly higher than the CPM ones. However, these differences were only of the order of a factor 2 to 3, and no differences were observed in the high energy region where the Urbach tails were almost exactly the same. Despite these small disagreements, Holovsky *et al.*

concluded that FTPS is an excellent alternative to the CPM to be used as a fast and reliable quantitative assessment of the quality of a-Si:H layers designed for photovoltaic absorbers.

3.3.3.b *Comparison of FTPS performed on thin films and solar cells*

As a fast characterization technique, FTPS could be used to compare the spectra obtained on thin films deposited on glass and on the solar devices incorporating the same films. Such a study was already done using CPM by P. Sladek *et al* [43] and these authors concluded that CPM was indeed a powerful tool to study the defect density in a-Si:H solar cells. We have repeated this experiment to check if the FTPS technique is as powerful as the CPM one, with the advantages of rapidity and high resolution. The complete study can be found in [44] and we shall concentrate here on the main results, illustrated by data obtained on one set of samples.

The a-Si:H thin films were deposited by means of a radio frequency powered plasma enhanced chemical vapor deposition (RF-PECVD) reactor with a pressure of 260 mTorr and an RF power of 4 W. These films were either deposited on glass and fitted with two parallel ohmic electrodes (1 cm long and 1 mm apart) for 'classical' FTPS measurements or incorporated into a solar cell. The coplanar film was approximately 2 µm thick. Concerning the cell, the back contact was made of a thick (1 µm) transparent conductive oxide (ZnO) deposited on glass on top of which a 20 nm thick n-doped layer of µc-SiO_x was deposited before the deposition of a 200 nm thick a-Si:H absorber. The device was completed by deposition of a 20 nm thick a-SiC:H p-doped layer and an 80 nm ZnO layer. This way, film and device were fully transparent, and we could perform measurements of the transmitted flux through them to minimize the influence of the interferences on the FTPS spectra. These spectra were measured with 100 V applied between the electrodes for the coplanar film, or under short circuit conditions for the device.

In order to normalize the FTPS spectra to estimate the absorption coefficient, we could have used the Ritter and Weiser formula (Eq. 3.6) or reflectance/transmittance measurements, but this technique cannot be used for solar devices, because the large number of interfaces, generating multiple reflections and transmissions, implies a more sophisticated treatment like, for instance, transfer matrix method (TMM). That is why the FTPS spectra were normalized to the external quantum efficiency (EQE), measured on the device using the part of our system dedicated to spectral response measurements [44].

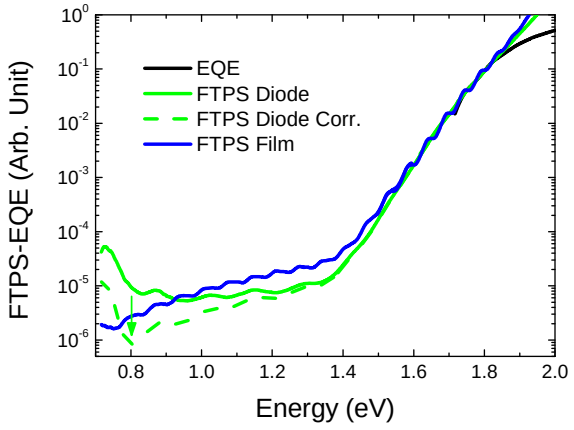

Figure 3.8. Full lines: FTPS spectra measured on a coplanar thin film and on a p-i-n diode with ZnO contacts, normalized to the EQE obtained with the device; Dashed line: FTPS spectrum of the device corrected for the absorptance of the ZnO contact deposited on glass. The arrow indicates the way the correction is acting (See text for details).

The results are displayed in Fig. 3.8. It can be seen that, because of the normalization to the transmitted flux, all the spectra are almost free from interferences and increase steeply in the high energy region (E > 1.8 eV), behaviors already seen previously. Both the film and the device present the same Urbach tail, with $E_u \approx 47$ meV, in the 1.4-1.8 eV energy range. The main discrepancies are found in the low energy region below 1.4 eV. The FTPS spectrum of the diode prepared with ZnO contacting layers is lower than the FTPS spectrum of the coplanar film for $1 \leq E \leq 1.4$ eV, whereas

below 1 eV, the FTPS spectrum of the diode increases to eventually cross the FTPS spectrum of the coplanar film. This behavior is quite surprising, since the FTPS spectra are expected to increase steadily from low energies to high energies, the number of transitions generating carriers increasing with the photon energy. To explain this behavior, we have to go back to the way the spectra are normalized.

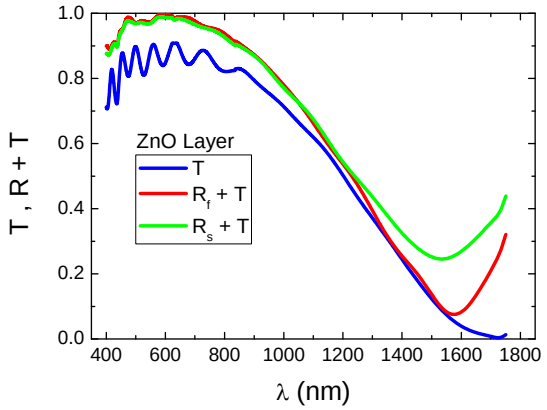

Figure 3.9. Transmittance T and the $R+T = 1-A$ of the ZnO layer used as contact in the device. R_f (R_s) is the reflectance measured illuminating the ZnO layer on the film (substrate) side.

The FTPS spectrum of the device has been obtained by normalizing its response to the flux transmitted through the complete device, including the contact deposited on glass. With our system, we have measured the transmittance and reflectance of this contact, the results being displayed in Fig. 3.9. It can be seen that the transmittance of ZnO is decreasing at long wavelengths, probably because of free carriers absorption linked to the metallic behavior of this film. Therefore, the flux transmitted through the device, with a transmittance T_{FTPS}, must be corrected to calculate the flux transmitted through the first ZnO layer and the a-Si:H film, with a transmittance T_{true} (see Fig. 3.10). Theoretically, this procedure would need a rather complicated treatment to derive the reflectance and transmittance of the complete stack or only the reflectance and transmittance of the TCO/aSi:H stack, like TMM for instance.

To simplify this procedure, and to correct, at least partly, the transmitted flux, we have taken into account the absorbance of the ZnO layers, A_{ZnO}, writing

$$T_{FTPS} = T_{True}\,(1 - A_{ZnO}) \quad , \qquad (3.19)$$

where

$$1 - A_{ZnO} = R_{ZnO} + T_{ZnO} \quad . \qquad (3.20)$$

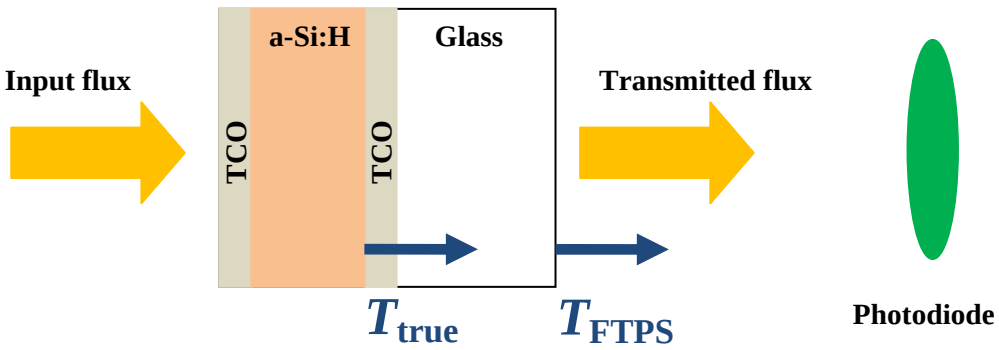

Figure 3.10. Schematic diagram of the measurement of the flux transmitted through the solar cells with transparent conductive oxide (TCO) electrodes.

Applying this very simple correction leads to the dashed curve displayed in Fig. 3.8, where it can be seen that, after correction, the FTPS spectrum measured on the devices is steadily increasing with energy from 0.8 eV, as expected, and parallels the spectrum obtained on the coplanar film.

Nevertheless, an increase of the FTPS spectrum with decreasing energy below 0.8 eV can still be noted in Fig. 3.8, indicating the limits of our simple method. A more refined method should be used for the deepest states. However, above 0.8 eV with our simple method it seems possible to correct the FTPS spectra recorded on a device to obtain very similar variations as the spectra recorded on a film.

It can be also noted that the deep defect density measured on a device is lower, by a factor of the order of 3, than the deep defect density measured on the film. A lower deep defect density obtained on devices compared to that of films had already been observed by Sladek *et al.* [43]. To explain this observation, these authors have first demonstrated that the quantum efficiency η was constant on the whole range of wavelengths investigated, so they have rejected the possibility of a variation of the generation linked to this parameter in the deep energy region. The interpretation of these authors was that as both types of carriers are generated, in devices the current is therefore limited by the carriers with the poorer transport properties, leading to an apparent lower density of states.

Another interpretation is that the deposition conditions may not be strictly identical for the isolated film and for the film in a device, since the coplanar film is deposited on an insulating substrate and the device film is deposited on a conductive one. Thus, we can think that the potential at the deposition surface is not the same in both cases, leading to a less defective layer when the substrate is conductive because of a smaller ion bombardment, for instance, and a smoother deposition.

In any case, and despite the fact that care has to be taken in the case of devices when normalizing the data to the transmitted flux, the FTPS proves to be an excellent means of systematic characterization of either films or devices. The technique is particularly useful for optimization of the deposition conditions or device architectures, since all the measurements presented here were achieved in a few minutes with the setup presented in Fig. 3.6, instead of the few hours required for CPM characterization.

3.3.c *Application of FTPS to the study of perovskite thin films*

The FTPS technique was applied to a large variety of thin films, such as a-Si:H, µc-Si:H, CIGS, diamond and organic semiconductors [15]. Surprisingly, only few publications deal with this powerful characterization technique applied to perovskite thin films [45]. Indeed, within a few years, the conversion efficiency of devices incorporating this material as an absorber has risen from a few % in 2009 to reach more than 25% at a laboratory scale [46]. However, despite this very fast progress, some issues remain to be fixed before this material can compete with the crystalline silicon industry [47, 48]. Among these issues, the stability of the material and device in outdoor conditions is obviously of crucial matter and, though it was only rarely used to characterize perovskite thin films, FTPS is an excellent tool to investigate on the combined influence of air and light on the opto-electronic properties of these films.

In this study, we have chosen to investigate some of the properties of triple-cation perovskite (methylamonium: MA, formamidinium: FA and Cs). The thin films were prepared from a $(MA_{0.17}FA_{0.83})Pb(Br_{0.17}I_{0.83})_3$ solution, also referred as MAFA. To form the desired triple perovskite, also referred as MAFACs, with formula $Cs_x(MA_{0.17}FA_{0.83})_{1-x}Pb(Br_{0.17}I_{0.83})_3$, the required quantity of Cs^+ was added from a stock precursor solution of CsI (Sigma Aldrich) 1.50 M in DMSO. Perovskite films were deposited by spin coating. Then, the samples were annealed at 100 °C during 30 min. All the films studied below presented a 5 % concentration of cesium and an excess of 10 % of PbI_2. More details on the preparation can be found in [49].

We have first studied the link between the FTPS spectra and the optical absorption coefficient α. Since for the same film the FTPS spectra can be obtained by normalization to the direct or the

transmitted flux, it seemed important to know which of these spectra provides the best match to the variations of α deduced from optical measurements. In Fig. 3.11a we present FTPS spectra obtained with normalization to the transmitted and the direct flux. Both spectra exhibit the same variations with photon energy from low energy up to 1.6 eV. Below 1.5 eV some deep states with a rather low density are present and above 1.5 eV the FTPS spectra rise steeply up to ~ 1.6 eV. The Urbach energy associated to this steep rise is $E_u \approx 17$ meV. Above 1.6 eV the two spectra present very different behaviors, the spectrum calibrated with the transmitted flux being largely above the spectrum calibrated with the direct flux.

The variation with energy of the absorption coefficient of the same film was measured with the transmittance/reflectance system of our bench, and, treated with the method of Poruba *et al.* [35] gives the curve presented in Fig. 3.11b (blue line). It can be seen that the best match is obtained with the FTPS spectrum normalized with the direct flux, and in the following we shall present only the FTPS spectra normalized to this flux.

We have studied the influence of light-soaking (LS) on the FTPS spectra, i. e., on the density of states, of a perovskite thin film. To light-soak the film with heavy light without heating it, we have used a high-power LED, the power density spectrum of which is shown in Fig. 3.12 and compared to the power density spectrum of the AM1.5G solar spectrum. It can be seen that the LED light is concentrated in the visible range of the solar spectrum and reaches a total power density of 0.44 kW/m^2, to be compared to the 1 kW/m^2 of the AM1.5 G spectrum. The fact that the LED light has no infrared component is not critical, since according to the FTPS spectra the light is not, or very weakly, absorbed by the perovskite film for wavelengths larger than 800 nm (energy lower than 1.55 eV).

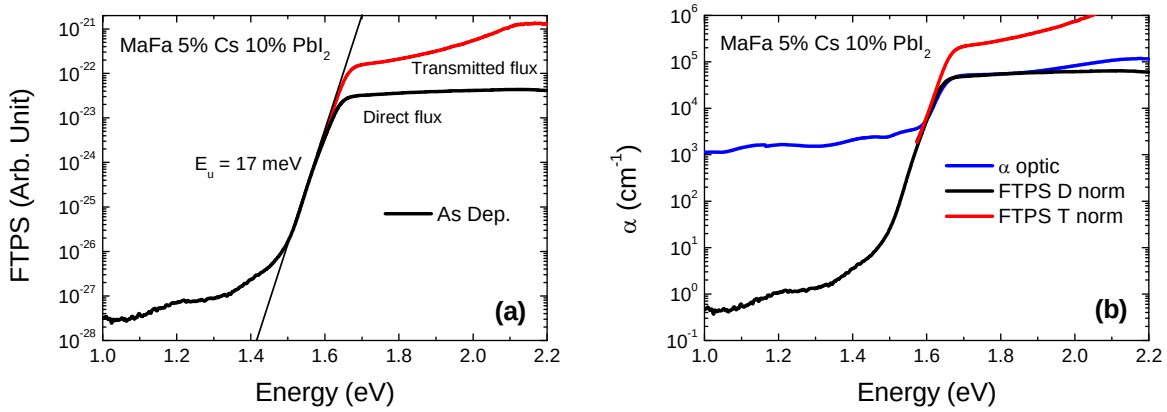

Figure 3.11. (a) FTPS spectra of an as deposited perovskite thin film obtained by normalization to the transmitted (red line) or direct (black line) flux, (b) Adjustment of the FTPS spectra to the absorption spectrum (blue line).

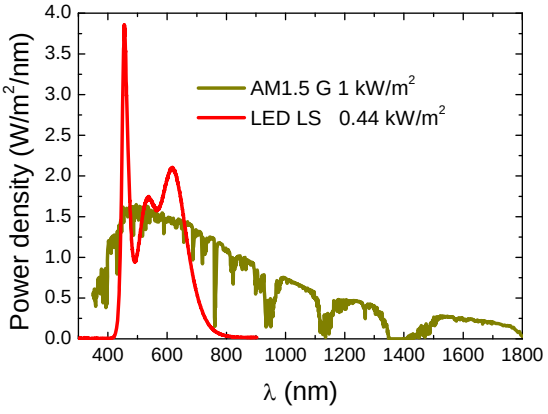

Figure 3.12. Power spectrum of the high-power LED used to light-soak the perovskite thin films (red line) compared to the AM1.5 G solar spectrum (yellow line).

In Fig. 3.13a we present the influence of light-soaking on a perovskite layer, the sample being maintained in the air. All the spectra have been normalized to the same value above 1.7 eV. It can be seen that there are no differences for the spectrum recorded on the sample being in the as-deposited state and on the same sample maintained under dark and primary vacuum (10^{-1} mBar) during 14 days. After 45 h of light-soaking the band edge is shifted toward low energies with no modification of the Urbach energy (red line), and after a recovery of 40 days under dark and primary vacuum the band gap has widen again (purple line). It is worth to note that the same type of sample left under air during some 65 hours did not present any evolution of the band gap when tested with the FTPS technique.

To quantify the evolution of the band gap with LS we have plotted the evolution of the Tauc gap [50]. This Tauc gap is calculated from the linear extrapolation toward the energy axis of the linear part of the plot of (FTPS data × photon energy)^2 versus photon energy, since the FTPS data are representative of the variations with energy of the absorption coefficient. These plots are presented in Fig. 3.13b and a clear evolution of the Tauc gap is observed with a value of E_g = 1.614 eV in the as-deposited state that decreases down to E_g = 1.597 eV after LS, and increases up to E_g = 1.621 eV after a recovery of 40 days.

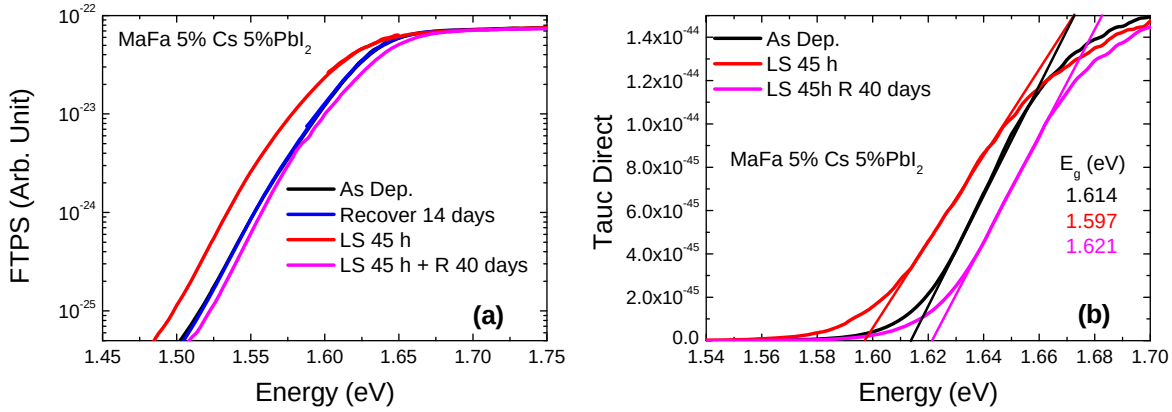

Figure 3.13. Evolution with time and light-soaking, (a) of the FTPS spectra, (b) of the Tauc gap of a perovskite thin film.

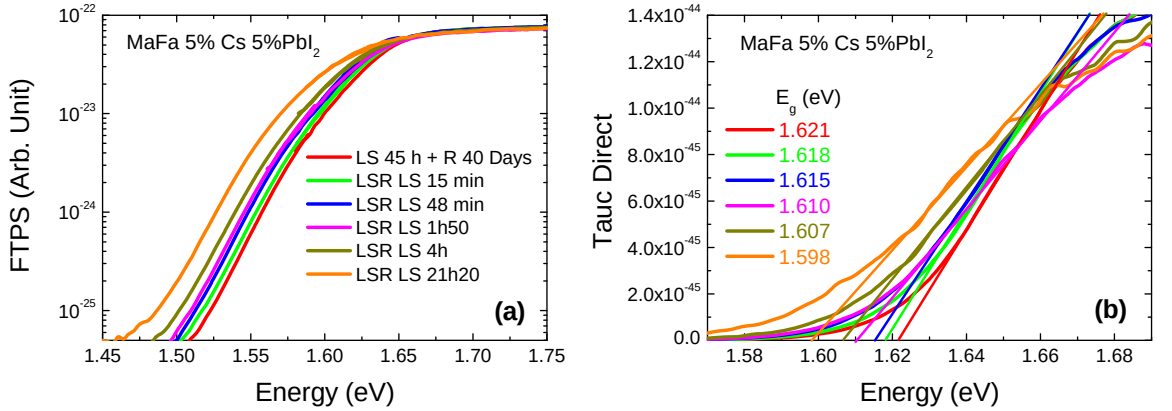

Figure 3.14. Evolution during a second light-soaking, (a) of the FTPS spectra, (b) of the Tauc gap of a perovskite thin film.

This LS experiment was repeated on the same sample with measurements of the FTPS spectra at different time intervals. The results are presented in Fig. 3.14a, all the FTPS spectra being normalized to the same value above 1.7 eV. It appears that the bang gap of the film is steadily decreasing with the LS time. From the plots of the Tauc gap, as we did previously, one can follow the

bang gap shrinking from 1.621 eV down to 1.598 eV from the recovered state to the new light-soaked state obtained after 21 hours (see Fig. 3.14b). According to these results, the evolution of the band gap with LS appears to be a reversible phenomenon. The reader may note that the evolution of the band gap with light-soaking was also observed with photoluminescence (PL) measurements performed simultaneously with FTPS. These PL measurements clearly showed that the maximum of the PL spectrum was shifting toward low photon energies with increasing light-soaking time as the gap of the sample was shrinking as revealed by FTPS [51]

Since we had observed a shrinking of the band gap with LS under air and no evolution of the gap under air alone, we have investigated on the influence of the air by achieving a LS under vacuum. Fig. 3.15a shows FTPS spectra obtained on the same film in the as-deposited state and after LS during 25 hours under vacuum. After normalization, as we did previously, it can be observed that the shrinking of the gap is extremely small and that, despite of the noise, the deep states down to 1.3 eV are also very similar. It is difficult to assess that there is an increase of the deep states below 1.3 eV, the signal to noise ratio being too low for an accurate measurement. On the other hand, a film with the same composition and light-soaked under air presents, as already seen, a shrinking of its band gap along with an increase of the deep defect density (see Fig. 3.15b). This increase of the deep defect density is clearly visible when one shifts upward by 40 meV the FTPS spectrum obtained after light-soaking (dashed blue curve): the Urbach energy remains the same but around 1.4 eV an increase of the FTPS spectrum by a factor of 3-4 is observed. Note that such an increase of the deep defect density upon LS was also reported by W. Tress [52]. As a conclusion, it seems that the shrinking of the band gap when the perovskite film is light-soaked under air is due to the combined influence of air and light, since a film left under air or a film light-soaked under vacuum does not present any evolution of the gap. This behavior underlines again that light and air have an influence on the perovksite films and that some issues remain to be fixed before perovskite could be used reliably in outdoor conditions under high illumination.

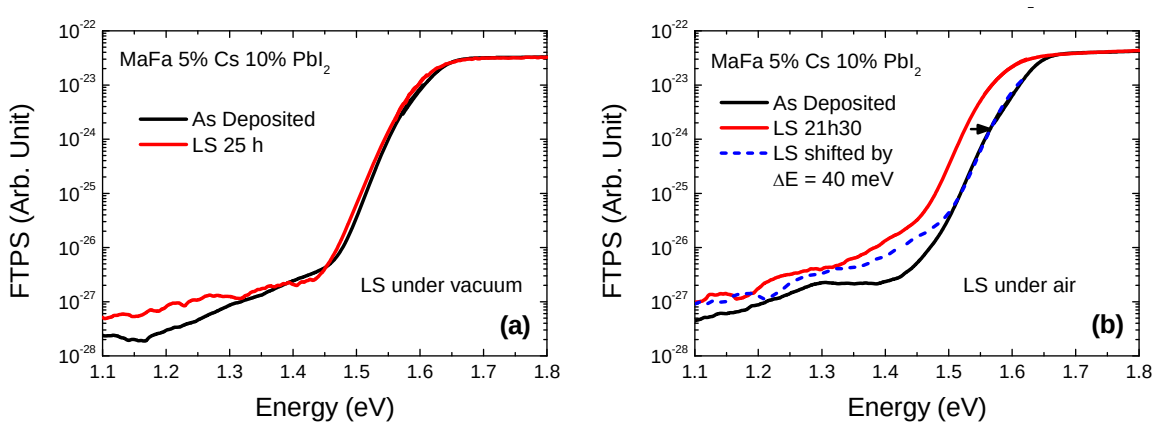

Figure 3.15. Evolution of the FTPS spectra of perovskite samples with light-soaking (a) under vacuum, (b) under air, the arrow indicates a shift of 40 meV upward of the LS spectrum.

3.4. Conclusion

Though the CPM seems apparently very simple in its principle, it appears particularly tricky to obtain reliable information on the defect density located in the band gap. For a-Si:H thin films, on one hand, all the authors seem to agree that the determination of the valence band tail distribution is accurate but, on the other hand, it was shown that the determination of the contribution of the deep states to the CPM spectrum may depend both on the model used to describe them (*e.g.* influence of the charged states, value taken for the matrix element…) and on the way the experiment is performed (*e.g.* level of the photocurrent taken as a reference, measurements in AC or DC modes, …). As far as deep

states are concerned, it seems that the determination of their distribution and concentration can only be done within a factor of two at the best. However, though an absolute determination of the deep DOS cannot be done accurately, comparative studies of their relative variations, with the deposition conditions or under heavy illumination, can be very fruitful. That is why the CPM technique was successfully applied for characterization of a-Si:H and μc-Si:H thin films, contributing largely to the optimization of the deposition conditions of these materials for solar energy conversion application.

However, CPM is a technique difficult to use for systematic characterization because of the time it takes to perform it. The FTPS is free from this flaw since the variations of the below-gap absorption coefficient with the photon energy can be recorded within a few seconds instead of hours. In addition, it was demonstrated that FTPS gives basically the same information as CPM and we have shown, as other groups, that it could be applied to solar devices. Therefore, FTPS appears as an excellent tool for systematic characterization of materials and devices, for instance to optimize the fabrication conditions under which solar devices are prepared to eventually obtain the best conversion efficiency. We have also shown that FTPS could be applied to the study of new and very promising materials as perovskites, in order to investigate on their stability. Indeed, perovskite stability is one of the key issues to be solved before solar devices based on this material could be applied in outdoor conditions with a sustainable reliability.

Appendix: Notations used for the most important quantities (by alphabetic order)

A	Absorptance	
d	Thickness of the sample	(cm)
E	Energy of the states	(eV)
E_C	Energy of the bottom of the conduction band	(eV)
E_F	Fermi level	(eV)
E_g	Band gap width	(eV)
E_u	Urbach energy	(eV)
E_V	Energy of the top of the valence band	(eV)
E_{04}	"Optical" band gap taken at $\alpha = 10^4$ cm^{-1}	(eV)
F	Flux of light	(cm^{-2}s^{-1})
$f(E)$	Occupation function of a monovalent state at the energy E under light	
G	Generation rate	(cm^{-3}s^{-1})
h	Planck constant	(4.136×10^{-15} eV s)
$h\nu$	Photon energy	(eV)
I_{dark}	Dark current	(A)
I_{ph}	Photocurrent	(A)
I_T	Total current	(A)
$N(E)$	Density of states at the energy E	(cm^{-3}eV^{-1})
N_C	Equivalent density of states at the bottom of the conduction band	(cm^{-3})
R	Reflection coefficient	
t	Time	(s)
T	Transmission coefficient	
q	Absolute value of the electronic charge	(1.60×10^{-19} C)
x	Depth in the film measured from the illuminated surface	(cm)
α	Absorption coefficient	(cm^{-1})
δ	Difference of the light paths in a Michelson interferometer	(cm)
Δn	Excess concentration of free electrons	(cm^{-3})

Δp	Excess concentration of free holes	(cm^{-3})
η	Quantum efficiency of the generation	
λ	Light wavelength	(cm)
μ_n	Extended states electron mobility	($cm^2V^{-1}s^{-1}$)
μ_p	Extended states hole mobility	($cm^2V^{-1}s^{-1}$)
ν	Frequency of the light	(Hz)
σ	Photoconductivity of the material	(Scm^{-1})
τ_n	Electron lifetime	(s)
τ_p	Hole lifetime	(s)
ω	Wavenumber associated to the light wavelength λ	(cm^{-1})

Acknowledgements

We thank Ouafa Saadane for the CPM measurements and Pere Roca i Cabarrocas from the Laboratoire de Physique des Interfaces et Couches Minces (LPICM, Palaiseau, France) for the deposition of a-Si:H and pm-Si:H films and devices. Many thanks to Amelle Rebai and Hung-Ju Lin from the Institut Photovoltaïque d'Ile de France (IPVF, Palaiseau, France) for the deposition of the perovskite thin films and to Michel Police and Richard Andlauer for technical assistance.

We thank the SOLSIA company for providing some of the a-Si:H samples in the framework of the POLYSIL project funded by the Agence de l'Environnement et de la Maîtrise de l'Energie (ADEME)

Part of this work was carried out under Ecos-Sud projects A02E01, A08E01, and A13E02.

References

1 Boccara, A. C., Fournier, D., Badoz, J. (1980) *Appl. Phys. Lett.* 36: 130.
2 Grimmeiss, H. G., Lebedo, L. A. (1975) *J. Appl. Phys.* 46: 2155.
3 Vaněček, M., Kocka, J., Stuchlik, J., Triska, A. (1981) *Solid State Comm.* 39: 1199.
4 Smith, Z. E., Chu, V., Shepard, K., Aljishi, S., Slobodin, D., Kolodzey, J., Wagner, S., Chu, T. L. (1987) *Appl. Phys. Lett.* 50: 1521.
5 Schmidt, J. A., Arce, R. D., Buitrago, R. H., Koropecki, R. R. (1997) *Phys. Rev. B* 55(15): 9621-9627.
6 Schmidt, J. A., Rubinelli, F. A. (1998) *J. Appl. Phys.* 83: 339-348.
7 Schmidt, J. A. Arce, R. D., Koropecki, R. R., Buitrago, R. H. (1999) *Phys. Rev. B* 59: 4568-4571.
8 Roy, D., Longeaud, C., Saadane, O. (2002) *J. Non-Cryst. Solids* 299-302: 511.
9 Kleider, J. P., Gauthier, M., Longeaud, C., Roy, D., Saadane, O., Brüggemann, R. (2002) *Thin Solid Films* 403-404: 188 - 192.
10 Poruba, A., Vaněček, M., Rosa, J., Feitknecht, L., Wyrsch, N., Meier, J., Shah, A., Repmann, T., Rech, B. (2001) in *Proceedings of the 17th European Photovoltaic Solar Energy Conference* (WIP, Munich, Germany): 2981.
11 Vaněček, M., Poruba, A. (2002) *Appl. Phys. Lett.* 80: 719.
13 Inushima, T., Brodsky, M. H., Kanicky, J., Serino, R. J. (1984) *AIP Conf. Proc.* 120 (AIP, New York): 24.
12 Tomm, J. W., Jaeger, A., Bärwolff, A., Elsaesser, T., Gerhardt, A., Donecker, J. (1997) *Appl. Phys. Lett.* 71: 2233.
14 Goris, L., Poruba, A., Hod'ákova, L., Vaněček, M., Haenen, K., Nesládek, M., Wagner, P., Vanderzande, D., De Schepper, L., Manca, J. V. (2006) *Appl. Phys. Lett.* 88: 052113.
15 Holovsky, J. (2011) in *Fourier Transforms-New Analytical Approaches and FTIR Strategies*, edited by G. Nikolic (IntechOpen), Chap. 13, available at http://www.intechopen.com/books/fourier-transforms-new-analytical-approaches-and-ftir-strategies/fourier-transform-photocurrent spectroscopy-on-non-crystalline-semiconductors.

16 Kocka, J., Vaněček, M., Triska, A. (1989). Energy and density of gap states in a-Si:H. In: *Amorphous Silicon and Related Materials* (Ed. H. Fritzsche), 297-327. Singapore: World Scientific.
17 Vaněček, M., Kocka, J., Poruba, A., Fejfar, A. (1995) *J. Appl. Phys.* 78: 6203.
18 Sasaki, M., Okamato, S., Hishikawa, Y., Tsuda, S. (1994) *Energy Mater. Sol. Cells* 34: 541.
19 Hishikawa, Y., Nakamura, N., Tsuda, S., Nakano, S., Kishi, Y. Kuwano, Y. (1991) *Jap. J. Appl. Phys.* 30: 1008.
20 Ritter, D., Weiser, K. (1986) *Optics comm.* 57: 336.
21 Vaněček, M., Kocka, J., Stuchlik, J., Kozisek, Z., Stika, O., Triska, A. (1983) *Solar Energy Mater.* 8: 411.
22 Kocka, J., Vaněček, M., Schamer, F. (1987) *J. Non- Cryst Solids* 97-98: 715.
23 Bouizem, Y. (1993). Etude de l'influence de l'Hydrogène sur les défauts et le désordre et sur les phénomènes de métastabilité dans le silicium amorphe hydrogéné. Pierre and Marie Curie University, Thesis.
24 Pierz, K., Mell, H., Terukov, J. (1985) *J. Non-Cryst. Solids* 77-78: 547.
25 Amato, G., Giorgis, F. (1993) *J. Appl. Phys.* 74: 3956.
26 Jensen, P. (1990) *Solid state Commun.* 76: 1301.
27 Jackson, W. B., Amer, N. M. (1982) *Phys. Rev. B* 25: 5559.
28 Bar-Yam, Y., Joannopoulos, J. D. (1987) *J. Non-Cryst. Solids* 97-98: 467-474.
29 Powell, M. J., Deane, S. C. (1993) *Phys. Rev. B* 48: 10815.
30 Wyrsch, N., Finger, F., McMahon, T. J., Vaněček, M. (1991) *J. Non-Cryst. Solids* 137-138: 347.
31 Pierz, K., Fuhs, W., Mell, H. (1991) *Phil. Mag. B* 63: 123-141.
32 Stradins, P., Frizsche, H., Tran, M. (1994) in "*Advanced Metallization for Devices and Circuits-Sciences, Technology, and Manufacturability*", edited by S. P. Mararka, A. Katz, K. N. Tu, and K. Maex, *MRS Symposia Proceeding* 337, Pittsburgh: 467.
33 Conte, G., Irrera, F., Nobile, G., Palma, F. (1993) *J. Non-Cryst. Solids* 164-166: 419.
34 Siebke, F., Yata, S., Hishikawa, Y., Tanaka, M. (1998) *J. Non Cryst.* 227-230: 977.
35 Poruba, A., Fejfar, A., Remeš, Z., Špringer, J., Vaněček, M., Kocka, J., Meier, J., Torres, P., Shah, A. (2000) *J. Appl. Phys.* 88: 148.
36 Sladek, P., Thèye, M. L. (1994) *Solid State Comm.* 89: 199.
37 Hasegawa, S., Nitta, S., Nonomura, S. (1996) *J. Non Cryst. Solids* 198-200: 544.
38 Main, C., Reynolds, S., Zrinscak, I., Merazga, A. (2004) *J. Non-Cryst. Solids* 338-340: 228-231.
39 Poruba, A., Vaněček, M., Meier, J., Shah, A. (2002) *J. Non-Cryst. Solids* 299-302: 536-540.
40 Puspitosari, N., Longeaud, C. (2017) *Rev. Sci. Instrum.* 88: 08611.
41 Persans, P. D. (1982) *Philos. Mag. B* 46: 435.
42 Holovsky, J., Poruba, A., Purkrt, A., Remes, Z., Vaněček, M. (2008) *J. Non-Cryst. Solids* 354: 2167-2170.
43 Sladek, P., St'ahel, P., Roca i Cabarrocas, P., Morin, P. (1998) *Phil. Mag. B* 77: 1049-1061.
44 Puspitosari, N., Longeaud, C., Lachaume, R., Zeyu, L., Rusli, Roca i Cabarrocas, P. (2017) *Phys. Status Solidi C* 14: 1700165.
45 De Wolf, S., Holovsky, J., Moon, S.-J., Löper, Ph., Niesen, B., Ledinsky, M., Haug, F.-J., Yum, J.-H., Ballif, C. (2014) *J. Phys. Chem. Lett.* 5: 1035-1039.
46 National Renewable Energy Laboratory (NREL) (2021), Research-Cell Efficiency Chart, https://www.nrel.gov/pv/cell-efficiency.html
47 Gräetzel, M. (2014) *Nat. Mater.* 13: 838-842.
48 Saliba, M. (2018) *Science* 359: 388.
49 Longeaud, C., Ramos, F. J., Rebai, A., Rousset, J. (2018) *Sol. RRL*: 1800192.
50 Tauc, J. (1968) *Materials Research Bulletin* 3: 37.
51 Lin, H.-J., Cacovich, S., Rebai, A., Rousset, J., Longeaud, C. (2020) *ACS Appl. Mater. Interfaces* 12: 19495−19503.
52 Tress, W., Yavari, M., Domanski, K., Yadav, P., Niesen, B., Corea Baena, J. P., Hagfeldt, A., Gräetzel, M. (2018) *Energy Environ. Sci.* 11: 151-165.